Low-Order Passivity-Based Robust Current Control Design for Grid-Tied VSCs

Javier Serrano-Delgado, *Graduate Student Member, IEEE*, Santiago Cobreces, *Member, IEEE*, Mario Rizo, *Member, IEEE*, and Emilio Jose Bueno, *Member, IEEE*

***Abstract*—This article presents a systematic robust current control design approach for three-phase voltage-source converters. Robustness is guaranteed by combining intrinsic passive properties of the impedance uncertainty at the point of common coupling together with stability results from a passivity-based control theory. This approach ensures stability against typical uncertainty sources at mid and high frequencies, such as cable resonances or other converters interaction, with significant less conservative performances than the obtained with the traditional robust control theory. The approach uses multiobjective controller synthesis formulation that allows us to logically combine robustness requirements with performance objectives avoiding heuristic iteration over the control structure and parameters. The controller synthesis is performed by means of a nonsmooth $\mathcal{H}_\infty$ optimization technique that tunes all free parameters of a vector-based controller function, which constraints its structure. This results in a synthesized controller with lower order than those obtained with convex optimization definitions of the $\mathcal{H}_\infty$ control problem. The design methodology is validated in time and frequency domain by means of theoretical analysis and experimental results with three usual grid filters: *L*, *LCL,* and *LLCL*.**

***Index Terms*—DC–AC inverters, $\mathcal{H}_\infty$ control, multiobjective tuning, passivity, resonances.**

Nomenclature

Signals

^{o}	Superscript for output disturbance.
^{r}	Superscript for reference signal.
e, x_r	Current controller error and resonator output.
i_{x}	Grid filter inductor currents ($\mathrm{x} = \{1, 2\}$).
$i_{\mathrm{pcc}}, u_{\mathrm{pcc}}$	PCC current and voltage.
p, q	Active and reactive powers.
u, u_Δ, w	Actuation, uncertainty, and disturbance inputs.
u_c	Grid filter capacitor voltage.
u_d, x_d	Discretization model output and states.
u_{fp}	Fundamental sequence filter output.
u_f	Antialiasing filter output.
v_{dc}	DC-bus voltage.
v_g	Grid Thevenin equivalent voltage.
y, y_Δ, z	Measured, uncertainty, and minimized outputs.
y_g, x_g	Grid filter measurements and states.

Parameters

$\gamma, \gamma_{\max}$	Best achieved and allowable soft constraint.
ω_0	Grid fundamental frequency.
ω_A, ω_{fp}	Antialiasing and sequence cut-off frequencies.
$\omega_{\mathrm{Bc}}, \omega_{\mathrm{Bm}}$	Critical and minimum control bandwidth.
ω_{Bdc}	DC-bus control bandwidth.
ω_B, ω_B^*	Achieved and desired control bandwidth.
ω_{p1}, ω_{p2}	Passivity excess lower and upper frequency.
C_{dc}	DC-bus capacitor.
$C_f, L_{\mathrm{x}}, R_{\mathrm{x}}$	Grid filter capacitor, inductor, and ESR ($\mathrm{x} = \{1, 2, 3\}$).
C_g, L_g, R_{lg}	Grid impedance capacitor, inductor, and ESR.
gH	Best achieved hard constraint.
$k_{\mathrm{pdc}}, k_{\mathrm{idc}}$	DC-bus proportional and integral gains.
k_{pr}	Passivity excess gain.
S_b, U_b	Base power and voltage.
T_d, T_s	Computational delay and sampling period.

Systems

$^{\mathcal{U}\to\mathcal{Y}}$	Superscript for subsystem from $\mathcal{U}$ to $\mathcal{Y}$.
Δ, Δ_N	Uncertainty and its passivity shortage part.
$\mathcal{G}$	Arbitrary system.
C_k, R_ω	Tunable subsystem and fixed resonator.
F_A, F_{fp}	Antialiasing and fundamental sequence filters.
G, Z_g	General control model and grid impedance.
G_g, G_d	Grid filter and discretization models.
K_c, G_f	Tunable gain matrix and feed-forward.
M, N	Closed loop of P and K, and M and Δ.
M_Δ, M_s	M subsystems for uncertainty and performance.
P, K	Generalized plant and synthesized controller.
S, S_c	Sensitivity of y to y^o and i_2 to i_2^o.
S_r, T	Tracking sensitivity and its complementary.
S_{ud}, S_{ur}	Sensitivity of u to u_{pcc} and u to i_2^r.
W_1, W_2, W_{pr}	Tracking, actuation, and passivity weights.
Y_F, Y	Input admittance with and without CRG.

Manuscript received September 3, 2020; revised January 24, 2021; accepted March 16, 2021. Date of publication March 23, 2021; date of current version June 30, 2021. This work was supported in part by the Spanish Ministry of Industry, Economy, and Competitiveness under Grant DPI2017-88505-C2-2-R, in part by the Spanish Ministry of Science, Innovation, and Universities under Grant RTI2018-098865-B-C33, and in part by the scholarship "Formacion de Profesorado Universitario." Recommended for publication by Associate Editor H. L. Ginn. *(Corresponding author: Javier Serrano-Delgado.)*

Javier Serrano-Delgado, Santiago Cobreces, and Emilio Jose Bueno are with the Department of Electronics, University of Alcala de Henares, 28805 Alcala de Henares, Spain (e-mail: javier.serranod@uah.es; santiago.cobreces@uah.es; emilio.bueno@uah.es).

Mario Rizo is with the Siemens Gamesa, 28830 Madrid, Spain (e-mail: mariorizomorente@gmail.com).

Color versions of one or more figures in this article are available at https://doi.org/10.1109/TPEL.2021.3068057.

Digital Object Identifier 10.1109/TPEL.2021.3068057

This work is licensed under a Creative Commons Attribution 4.0 License. For more information, see https://creativecommons.org/licenses/by/4.0/

I. Introduction

THE increasing presence of voltage-source converters (VSCs) in power systems has placed its stability against grid uncertainties under intense study [1], [2]. One of the main sources of uncertainty, due to the interaction with other VSCs connected to the point of common coupling (PCC) and intrinsic parameters in transformers and electric connections, is the equivalent grid impedance. The design of inner control loops for VSCs that are compatible with the equivalent grid impedance is a key topic in avoiding instability or undesired oscillations [3], [4].

When an accurate model of the grid impedance is available, the straight-forward option is to integrate its dynamics into the plant model and design VSC controllers using standard control techniques as expressed in [5] and [6]. However, in practice, the lack of information at each PCC limits its knowledge to a range of possible values in a simplified dynamic model. In that situation, the conventional robust control theory [7] gives an approach to this problem relying on the compliance with the small gain theorem using $\mathcal{H}_\infty$ control [8]. The basic idea behind that approach is to quantify uncertainty in terms of gain bounds and design a controller to stabilize the system in a worst case scenario that is valid for any other situation. However, its conservativeness often leads to poor closed-loop performances when high uncertainty appears at a given frequency range.

Alternatively, passivity-based robust control (PBRC) approach may lead to less conservative results by assuming certain gain and phase properties in the uncertainty, as demonstrated in [9]. Hence, the controller design gives the closed-loop system dynamic features that ensure stability by compliance with the passivity theorem, which, along with the small-gain theorem, are corollaries of the sector stability theorem [10]–[14]. It will be shown that, when applied to the VSC current control problem, this approach amounts to render controllers that induce passivity-related conditions over converter input admittance. While this input admittance around the grid fundamental frequency is mainly determined by outer controllers [4], [15]–[17], the inner controller is the main responsible for it out of that frequency band at mid and high frequencies, where significant instability problems have been identified related to resonances [18]. The importance of converter input admittance on grid local stability has motivated an important research effort in recent years that has been translated into useful proposals from both classic and modern control design points of view.

Most classic design approaches propose to modify an already existing controller, designed to achieve tracking and standalone stability requirements, to get the desired passivity properties on the closed-loop admittance. For instance, passivity shortage at high frequency due to time delays has been proposed to be compensated by an appropriate PCC voltage feed-forward [3], [19] or biquad filters inside the current loop [20]. Also, Xie *et al.* [21] showed how relevant the *LCL* grid filters design is for closed-loop passivity assessment. The main limitations of these methods are their increasing design involvement, when either plant dynamics or design requirements are complex, and possible performance deterioration.

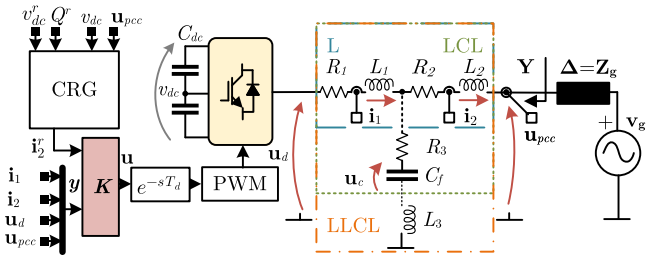

Fig. 1. Single-phase equivalent of a current-controlled grid-tied VSC with several grid filters (*L*, *LCL*, *LLCL*) facing an uncertain grid impedance $Z_g(s)$ expressed by its Thevenin equivalent at the PCC.

Modern approaches try to transfer that design complexity into a computational tool, by relying on modern optimization techniques, allowing the designer to focus on problem specification. Model-reference $\mathcal{H}_\infty$ has been proposed [22], [23] as an indirect alternative to achieve closed-loop passivity by mimicking a passive dynamic model: When the result is close to the reference model, its passivity is inherited. Still, the absence of an actual passivity constraint for synthesis induces a lack of design guarantees and some conservativeness on the results. Besides, from a practical and numerical point of view, as most $\mathcal{H}_\infty$ designs, the synthesized controllers are of high order—it encapsulates the order from plant and frequency-domain specifications.

The passivity constraint along with performance requirements lead to multiobjective controller synthesis approaches. The main theoretical approach is based on linear matrix inequalities (LMIs) derived from positive-real lemma and bounded-real lemma [24]. This approach requires convex optimization-based controller synthesis that, unfortunately, presents important practical problems as an inherent conservativeness [25] and, again, high-order resulting controllers that are prone to numerical instability.

This article considers a close but alternative procedure that relies on nonsmooth optimization techniques [26], [27], which have been successfully applied in other problems [28], [29] to find feasible solutions. This approach allows evaluating and enforcing of the required passivity constraint and performance objectives [14] to tune the selected controller structure. Then, this proposal is a systematic robust control tuning methodology with lower order and conservativeness.

The analyzed problem consists on the design of a current controller for a VSC-connected through several grid filters topologies (*L*, *LCL*, and *LLCL*) to a grid with uncertainty. Fig. 1 depicts a simplified diagram of the electrical topology and fundamental control structure including the current reference generation (CRG), which is required for workability on a practical application, but ineffective at mid and high frequencies.

Authors have already researched on this path in [30]. This article presents improvements and contributions in the following aspects. It introduces the possibility of applying the method to uncertainties that are not completely passive, it reduces the design process to a single-step procedure that minimizes

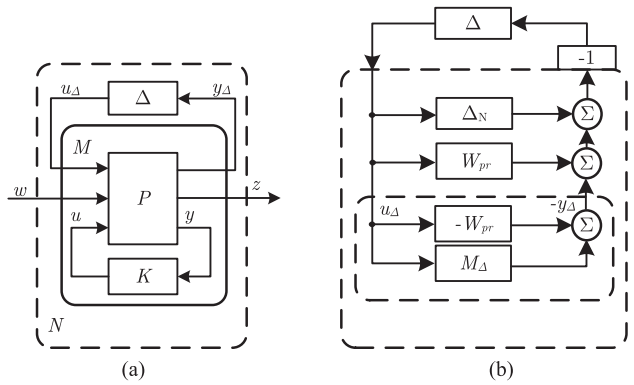

Fig. 2. (a) M–Δ structure for robust stability analysis. (b) Model modification for PBRC assessment when Δ is passive and the system to be controlled M_Δ is paralleled with another uncertain system Δ_N with a passivity shortage.

iterations, it allows the synthesis of low-order industry-suitable fixed-structure controllers, and it extends the design to other usual grid filter topologies.

The rest of this article is organized as follows. Section II makes a brief review of the theoretical basis of the proposal, justifying why robust control design can be formulated inside the passivity control framework. Section III describes the plant and characterizes the uncertainty. Section IV presents the multiobjective current controller tuning methodology for PBRC. Section V describes several design study cases together with a complete analytical and experimental validation. Finally, Section VI concludes the article, followed by the Appendix.

II. Theoretical Background

A. Control Problem Definition

The control proposal will be approached within the framework of the generalized control problem shown in Fig. 2(a) [31]. The generalized plant $P(s)$ is a dynamic multiple-input multiple-output (MIMO) model composed of the system to be controlled and interconnected weighting functions that serve as a vehicle to translate design(er) control objectives into a design problem. Variables u and y define the input–output structure of the controller. The relationship between w and z defines the performance objectives.

Besides, block $\Delta(s)$[1] represents an unknown dynamic model that is, in fact, the part of the system to be controlled that is not (correctly) modeled. For this purpose, without loss of generality, the uncertain model is necessarily expressed as a feedback system, from y_Δ to u_Δ.

The robust control strategy amounts, then, to find a controller K such that the closed-loop system[2] $M = F_l(P, K)$ fulfills some performance objectives, expressed as gain bounds between input w and output z, while ensuring that $N = F_u(M, \Delta)$ is stable for a set of uncertainty models Δ.

[1]For notation simplicity, the complex variable s will be omitted when it results obvious from the context.

[2]The notations F_u and F_l denote the upper and lower linear fractional transformations (LFT), respectively.

B. Passivity-Based Robust Control

This section is dedicated to briefly review some key concepts regarding passivity and how can be used to face the robust control problem. Passivity or positive realness, which are equivalent for linear time-invariant (LTI) systems, is defined as follows.

Definition 1 (Positive Real Transfer Function [9], [32]): A transfer function $\mathcal{G}(s)$ is passive or positive real if 1) $\mathcal{G}(s)$ is analytic in $\Re(s) > 0$, and 2) $\mathcal{G}(j\omega) + \mathcal{G}^*(j\omega) \geq 0 \, \forall \, \omega \in \mathbb{R}$ and $j\omega$ is not a pole[3] of $\mathcal{G}(s)$. The transfer function is strictly passive or positive real if $\mathcal{G}(j\omega) + \mathcal{G}^*(j\omega) > 0 \, \forall \, \omega \in \mathbb{R}$.

Passive systems, from an input–output point of view, deliver less (or equal[4]) energy than they are supplied with. Its interest in control theory is, in part, motivated by the strong results on stability of connected passive systems: The parallel connection of passive subsystems is passive while their feedback interconnection leads to the passivity theorem.

Proposition 1 (Passivity Theorem for Linear Systems [9]): The closed-loop system is asymptotically stable, if the forward path LTI subsystem is strictly passive, and the feedback path LTI subsystem is passive.

This proposition is the basis of PBRC: In Fig. 2(a), if $M_\Delta = -M^{u_\Delta \to y_\Delta}$ is strictly passive, N will be stable for any passive Δ. In practical problems, however, it may happen that Δ is not passive. For those situations, the result can be extended to connections comprising passive and nonpassive subsystems. The concepts of excess and shortage of passivity, by means of indices, give a measure of how (non)passive a system is.

Definition 2 (Input Feedforward Passivity (IFP) Index [9]): The IFP index for a stable linear system $\mathcal{G}(s)$ at frequency ω is defined as

$$\nu_F(\mathcal{G}(s), \omega) \triangleq \frac{1}{2} \, \underline{\lambda}(\mathcal{G}(j\omega) + \mathcal{G}^*(j\omega)) \tag{1}$$

where $\underline{\lambda}$ denotes the minimum eigenvalue. Then, the IFP index is $\nu(\mathcal{G}(s)) \triangleq \min_{\omega \in \mathbb{R}} \nu_F(\mathcal{G}(s), \omega)$.

From the previous definition, a linear system is strictly passive if it is stable and $\nu > 0$. The output feedback passivity (OFP) index [9] is not used in this article.

If the uncertainty has a passivity shortage, that is $\nu(\Delta) < 0$, the robust stability condition for M_Δ changes. For general control problems, Bao and Lee [9] presented a positive feedback weighting function $W_{pr}(s)$ that expresses a generalized excessive OFP condition over M_Δ to ensure robustness. Alternatively, in specific uncertainty cases, Δ can be broken down into uncertain subsystems with passivity shortage, so that a generalized excessive IFP condition over M_Δ is required.

Proposition 2: Assume that $\Delta(s)$ is passive, and $\Delta_N(s)$ is stable with $-\nu_F(\Delta_N(s), \omega) \leq \nu_F(W_{pr}(s), \omega) \, \forall \, \omega \in \mathbb{R}$, where $W_{pr}(s)$ is stable and minimum phase. The feedback system

[3]If there are poles of $\mathcal{G}(s)$ on the imaginary axis, they are nonrepeated and the residue matrix at the poles is Hermitian and positive semidefinite. Note that $\mathcal{G}^*(j\omega)$ is the complex conjugate transpose of $\mathcal{G}(j\omega)$.

[4]Systems delivering strictly less energy are namely *strictly passive* while *passivity* includes the equality.

$F_u(-M_\Delta - \Delta_N, \Delta)$ is stable, if $M_\Delta(s) - W_{pr}(s)$ is stable and strictly passive.

The proof can be derived considering Fig. 2(b), Proposition 1, and Definition 2. In the following, W_{pr} is encapsulated in P, so that $M^{u_\Delta \to y_\Delta}$ is redefined including the sum of W_{pr}.

These objectives can be formally expressed as a constrained optimization problem

$$\begin{aligned} \underset{K}{\text{minimize}} \quad & \|M_s(s)\|_\infty = \max_\omega \overline{\sigma}(M_s(j\omega)) \\ \text{subject to} \quad & M_\Delta(s) \text{ is strictly passive} \end{aligned} \tag{2}$$

where $M_s = M^{w \to z}$ and $\overline{\sigma}$ denotes the maximum singular value. Generally, a good performance objective achievement is $\|M_s\|_\infty \leq 1$.

Finally, an alternative measure of passivity, used by some computational tools, is the relative passivity index (*R*-index).

Definition 3 (Relative Passivity Index (R-index) [33]): The *R*-index for $\mathcal{G}(s)$ at frequency ω when $I + \mathcal{G}(s)$ is minimum phase is defined as

$$R_F(\mathcal{G}(s), \omega) \triangleq \overline{\sigma}\left([I - \mathcal{G}(j\omega)] [I + \mathcal{G}(j\omega)]^{-1} \right). \tag{3}$$

Then, the *R*-index is $R(\mathcal{G}(s)) \triangleq \max_{\omega \in \mathbb{R}} R_F(\mathcal{G}(s), \omega)$.

Hence, $\mathcal{G}(s)$ is passive if $R_F < 1$, and $R_F > 1$ denotes a passivity shortage.

C. Controller Synthesis Approaches

There are two main strategies in the literature to synthesize passive systems using feedback loops, as required by Proposition 2 and (2): the direct use of the Positive-Real Lemma [25], or, alternatively, the use of *Cayley Transformation*, which allows us to transform that problem into an $\mathcal{H}_\infty$ synthesis problem [34].

Positive-real lemma implies an optimization problem with LMIs, which give, also, the possibility of simultaneously including $\mathcal{H}_\infty$ performance requirements using the bounded real lemma [25]. However, the stacking of both conditions may introduce enough conservativeness in the problem to make the synthesis impossible in some practical applications [24], [25], [35]. In our experience, this approach is, for that reason, invalid for the problem here studied.

Then, Lemma 1 provides the alternative approach that transforms the problem into a multichannel $\mathcal{H}_\infty$ problem.

Lemma 1 (Cayley transformation [34]): Let the Cayley transformation of $\mathcal{G}(s)$ be given by

$$\mathcal{G}'(s) = [I - \mathcal{G}(s)] [I + \mathcal{G}(s)]^{-1}. \tag{4}$$

Then, $\mathcal{G}(s)$ is positive real if and only if $\mathcal{G}'(s)$ is stable and $\|\mathcal{G}'(s)\|_\infty \leq 1$.

This transformation is expressed by feedback and feedforward operations, as depicted in Fig. 3. The generalized plant P is divided, then, into two models: the performance model $P^{[w^T, u^T]^T \to [z^T, y^T]^T}$, and the passivity model $P^{[u_\Delta^T, u^T]^T \to [y_\Delta^T, y^T]^T}$ with its *Cayley transformation*, (see Appendix A). Then, the performance channels are unaffected by the transformation.

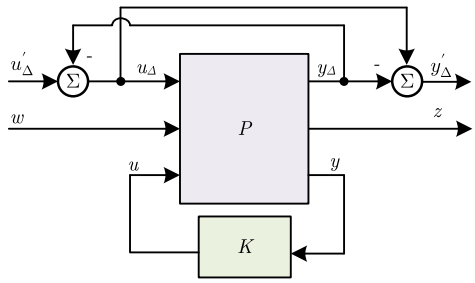

Fig. 3. Generalized plant P transformation for controller synthesis with passivity enforcement using *Cayley transformation*.

Once the problem has been converted into an $\mathcal{H}_\infty$ optimization problem, there are, again, several alternative algorithms to extract the final controller. If the system under analysis is reasonably complex, convex optimization tools are attractive due to their theoretical convergence guarantees. In practice, however, the resulting controller inherits the order of plant P without any interesting internal structure.

Alternatively, nonconvex optimization techniques, based on first-order descent methods, are increasing their acceptance in practical control scenarios [26], [27]. These techniques offer full flexibility to designers by keeping controller complexity low [28] and allowing structures closely attached to the physical quantities. This is very useful for industrial applications. Besides, their theoretical lack of convergence guarantees does not seem to represent an actual problem, in authors' experience. The obtained results are very close to the optimal and well-conditioned, which gives better practical performances than those obtained by convex approaches.

In this framework, the function to be minimized, or *soft* requirement, encapsulates the performance objective in (2), whereas the design constraint, or *hard* requirement, enforces passivity. The controller has to satisfy *hard* constraints to be acceptable, so that the local solution is a locally optimal controller in the set of *hard* constraints feasible controllers. This tool is implemented in MATLAB routines `hinfstruct` and `systune` [29], [33].

III. Grid-Tied Current-Controlled VSCs

This article analyzes the VSC control problem using complex-valued LTI systems and signals that can be derived from symmetrical three-wire three-phase electrical systems by modeling them using space vectors [16], [36].[5] By default, the space vector is in stationary reference frame (StRF, $\alpha\beta$). Any complex-valued LTI system $\boldsymbol{\mathcal{G}}(s)$ may be equivalently defined as a real-valued one $\mathcal{G}(s)$, so that all definitions in Section II are still valid for our case under study.

[5]We have followed the notation in [16] real-valued single-input single-output (SISO) and MIMO systems and signals are denoted by italic letters; complex-valued SISO systems and signals are denoted by bold letters; complex-valued MIMO systems and vector signals are denoted by bold-italic letters.

TABLE I
GRID FILTER MODELS

Grid filter	$\boldsymbol{x}_g$	$\boldsymbol{A}_g$	$\boldsymbol{B}_{vg}$	$\boldsymbol{B}_{ug}$
L	$\begin{bmatrix}\mathbf{i}_2\end{bmatrix}$	$\begin{bmatrix}-(R_1+R_2)/(L_1+L_2)\end{bmatrix}$	$\begin{bmatrix}-1/(L_1+L_2)\end{bmatrix}$	$\begin{bmatrix}1/(L_1+L_2)\end{bmatrix}$
LCL[1] LLCL[2]	$\begin{bmatrix}\mathbf{i}_1\\ \mathbf{i}_2\\ \mathbf{u}_c\end{bmatrix}$	$\begin{bmatrix}-[(R_1+R_3)L_2+L_3R_1]/L_c & (L_2R_3-L_3R_2)/L_c & -L_2/L_c\\ (L_1R_3-L_3R_1)/L_c & -[(R_2+R_3)L_1+L_3R_2]/Lc & L_1/L_c\\ 1/C_f & -1/C_f & 0\end{bmatrix}$	$\begin{bmatrix}-L_3/L_c\\ -(L_1+L_3)/L_c\\ 0\end{bmatrix}$	$\begin{bmatrix}(L_2+L_3)/L_c\\ L_3/L_c\\ 0\end{bmatrix}$

[1]For this case $L_3 = 0$ and $L_c = L_1L_2$.
[2]For this case $L_c = L_1L_2 + L_1L_3 + L_2L_3$.

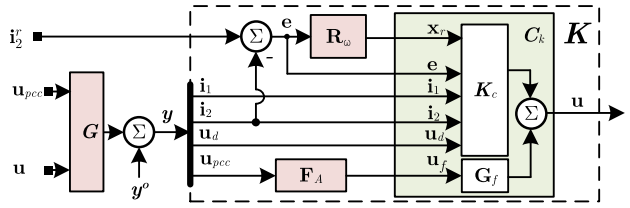

Fig. 4. Closed-loop model with detailed definition of the structure of $\boldsymbol{K}$ dividing in fixed ($\mathbf{R}_\omega$ and $\mathbf{F}_A$) and tunable parts ($\boldsymbol{C}_k$).

A. Plant Model

The VSC is connected to the grid through several grid filter topologies, see Fig. 1, with the following general model $\boldsymbol{G}(s)$:

$$\begin{bmatrix}\dot{\boldsymbol{x}}_g\\ \dot{\boldsymbol{x}}_d\\ \boldsymbol{y}_g\\ \mathbf{u}_d\\ \mathbf{u}_{\text{pcc}}\end{bmatrix} = \left(\begin{array}{cc|cc} \boldsymbol{A}_g & \boldsymbol{B}_{ug}\boldsymbol{C}_d & \boldsymbol{B}_{vg} & 0\\ 0 & \boldsymbol{A}_d & 0 & \boldsymbol{B}_d\\ \hline \boldsymbol{C}_g & 0 & 0 & 0\\ 0 & \boldsymbol{C}_d & 0 & 0\\ 0 & 0 & 1 & 0\end{array}\right)\begin{bmatrix}\boldsymbol{x}_g\\ \boldsymbol{x}_d\\ \mathbf{u}_{\text{pcc}}\\ \mathbf{u}\end{bmatrix} \tag{5}$$

where the matrices and states of $\boldsymbol{G}_g(s)$ are summarized in Table I and the measured variables are $\boldsymbol{y}_g = \mathbf{i}_2$ for L filter or $\boldsymbol{y}_g = [\mathbf{i}_1, \mathbf{i}_2]^T$ for *LCL* and *LLCL* filters, so that $\boldsymbol{C}_g$ has the appropriate value and dimensions. The computational delay plus zero-order-hold (ZOH) and sampler model is defined as

$$\mathbf{G}_d(s) = e^{-sT_d}\frac{1-e^{-sT_s}}{sT_s} \tag{6}$$

where $T_d = T_s$ and the state-space matrices by approximating each exponential term with a second-order Pade are

$$\boldsymbol{A}_d = \begin{pmatrix}-12/T_s & 1 & 0 & 0\\ -60/T_s^2 & 0 & 1 & 0\\ -144/T_s^3 & 0 & 0 & 1\\ -144/T_s^4 & 0 & 0 & 0\end{pmatrix}\quad \boldsymbol{B}_d = \begin{pmatrix}0\\ 12/T_s^2\\ -72/T_s^3\\ 144/T_s^4\end{pmatrix}$$
$$\boldsymbol{C}_d = \begin{pmatrix}1 & 0 & 0 & 0\end{pmatrix}.$$

The dynamics of $\mathbf{i}_2$, see Fig. 4, are

$$\mathbf{i}_2 = \underbrace{\boldsymbol{S}^{\boldsymbol{y}^o\to\mathbf{i}_2}\boldsymbol{G}^{\mathbf{u}\to\boldsymbol{y}}\mathbf{K}^{\mathbf{i}_2^r\to\mathbf{u}}}_{\mathbf{T}(s)}\mathbf{i}_2^r + \underbrace{\boldsymbol{S}^{\boldsymbol{y}^o\to\mathbf{i}_2}\boldsymbol{G}^{\mathbf{u}_{\text{pcc}}\to\boldsymbol{y}}}_{-\mathbf{Y}(s)}\mathbf{u}_{\text{pcc}} \tag{7}$$

where $\boldsymbol{S} = [I - \boldsymbol{G}^{\mathbf{u}\to\boldsymbol{y}}\boldsymbol{K}^{\boldsymbol{y}\to\mathbf{u}}]^{-1}$. Note that each term of $\boldsymbol{y}^o$ has the same nature as the corresponding one in $\boldsymbol{y}$ for sensitivity analysis purposes. The inputs of $\boldsymbol{K}$ are $\mathbf{i}_2^r$ and output signals of $\boldsymbol{G}$.

B. Current Controller Structure

The controller structure depends on the control objectives. Our case of study requires to track a given current reference $\mathbf{i}_2^r$, with zero steady-state error, a damped response for step changes when there is no grid impedance and good standalone stability margins. This proposal must also render $\mathbf{Y}$, so that it complies with the passivity requirements derived from Proposition 2. The proposed structure for such objectives is a 2 degree-of-freedom (DOF) controller with PCC voltage feed-forward, see Fig. 4.

Each measured grid filter current as well as the delayed control action $\mathbf{u}_d$ has its corresponding gain. The error $\mathbf{e} = \mathbf{i}_2^r - \mathbf{i}_2$ goes through an additional proportional gain and a resonator $\mathbf{R}_\omega$ with infinite gain at ω_0, which is the frequency of the signal to be tracked. The resonator for continuous-time controller synthesis is

$$\mathbf{R}_\omega(s) = \frac{1}{s - j\omega_0}. \tag{8}$$

The tunable part $\mathbf{G}_f(s)$ has an arbitrary order and it is added because it has admittance shaping capabilities at mid and high frequencies. For simplicity, this article will consider a null imaginary part, that is $\Im(\mathbf{G}_f) = 0$.

In practice, $\mathbf{u}_{\text{pcc}}$ must be filtered for L grid filters when the grid is considerably weak. Then, $\mathbf{F}_A$ removes the switching harmonics beyond ω_A.

In order to ensure that the solutions are reachable, the fixed parts of $\boldsymbol{K}$, that is $\mathbf{R}_\omega$ and $\mathbf{F}_A$, are absorbed into $\boldsymbol{P}$ keeping only the low-level tunable parameters in $\boldsymbol{C}_k$. Then, $\boldsymbol{C}_k$ is composed of a tunable constant matrix $\boldsymbol{K}_c$, whose input vector is organized as $\begin{bmatrix}\mathbf{x}_r, \mathbf{e}, \mathbf{i}_1, \mathbf{i}_2, \mathbf{u}_d\end{bmatrix}$, and tunable matrices of $\mathbf{G}_f$, that is $\boldsymbol{A}_f$, $\boldsymbol{B}_f$, $\boldsymbol{C}_f$, and $\mathbf{D}_f$.

The addition of the ZOH and sampler effects in model $\boldsymbol{G}$ allows the discrete-time implementation of this controller with a few steps: $\mathbf{G}_f$ is discretized using a bilinear (Tustin) transformation; $\boldsymbol{K}_c$ does not require any transformation; and the discrete-time resonator implementation to exactly match the frequency domain behavior at low frequency is

$$\mathbf{R}_\omega(z) = \frac{(e^{j\omega_0T_s} - 1)/(j\omega_0)}{z - e^{j\omega_0T_s}}. \tag{9}$$

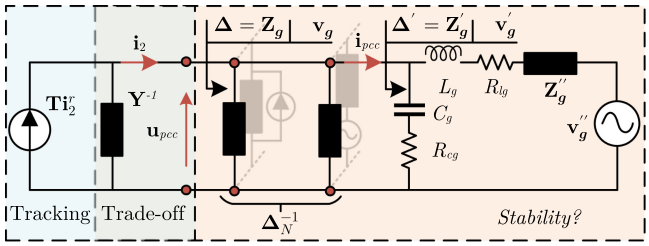

Fig. 5. Current-controlled VSC facing PCC uncertainty (from left to right): several paralleled VSCs with equivalent admittance identified as $\mathbf{\Delta}_N$; *LC*-type cable model; remaining grid given by $\mathbf{Z}_g''$ and voltage $\mathbf{v}_g''$.

Note that this controller can be transformed into a synchronous reference frame (SRF) by transforming $\mathbf{R}_\omega(z)$ to $\mathbf{R}_\omega(ze^{j\omega_0 T_s})$.

C. Current Reference Generation

The reference $\mathbf{i}_2^r$ must be appropriately generated to synchronize the VSC with the grid using additional algorithms. Let us indicate that these algorithms are out of the PBRC analysis, and they are indicated for experimental workability purposes.

The voltage v_{dc} is controlled using the control law

$$p^r = (k_{\text{pdc}} + k_{\text{idc}}/s)({v_{\text{dc}}^r}^2 - v_{\text{dc}}^2) - k_{\text{pdc}} v_{\text{dc}}^2 \tag{10}$$

where $k_{\text{pdc}} = -\omega_{\text{Bdc}} C_{\text{dc}}/2$ and $k_{\text{idc}} = -\omega_{\text{Bdc}}^2 C_{\text{dc}}/2$ by using a classic energy balance approach [37].

Then, the current reference is derived from the instantaneous power equations for three-phase three-wire systems using Clarke transformation [38] as follows:

$$\begin{bmatrix} \Re(\mathbf{i}_2^r) \\ \Im(\mathbf{i}_2^r) \end{bmatrix} = \frac{2/3}{|\mathbf{u}_{fp}|} \begin{pmatrix} \Re(\mathbf{u}_{fp}) & \Im(\mathbf{u}_{fp}) \\ \Im(\mathbf{u}_{fp}) & -\Re(\mathbf{u}_{fp}) \end{pmatrix} \begin{bmatrix} p^r \\ q^r \end{bmatrix} \tag{11}$$

where $|\mathbf{u}_{fp}| = \sqrt{\Re(\mathbf{u}_{fp})^2 + \Im(\mathbf{u}_{fp})^2}$ and $\mathbf{u}_{fp}$ is the filtered version of $\mathbf{u}_f$ to ensure that we generate a reference with just the fundamental. The filter is the frequency-shifted version of a first-order low-pass filter

$$F_{fp}(s) = \frac{\omega_{fp}}{s - j\omega_0 + \omega_{fp}} \tag{12}$$

where ω_{fp} defines the bandwidth. Expressions (11) and (12) define the current reference calculator (CRC).

D. Characterization of Uncertainty

When the VSC faces a PCC with voltage $\mathbf{v}_g$ and completely unknown impedance, $\mathbf{\Delta} = \mathbf{Z}_g$, the dynamics of the output current change to

$$\mathbf{i}_2 = [I + \mathbf{Y}\mathbf{\Delta}]^{-1}\mathbf{T}\mathbf{i}_2^r - [I + \mathbf{Y}\mathbf{\Delta}]^{-1}\mathbf{Y}\mathbf{v}_g. \tag{13}$$

The considered uncertainty $\mathbf{\Delta}$, as depicted in Fig. 5, is used to model several usual uncertainty sources: equivalent admittance at the PCC of several paralleled VSCs, which is indicated as $\mathbf{\Delta}_N$, with bounded passivity shortages; and a Thevenin equivalent with passive impedance, $\mathbf{\Delta}' = \mathbf{Z}_g'$. The latter can be also broken down into an *LC*-type cable model to analyze possible resonance uncertainty and another Thevenin equivalent of the rest of the grid with impedance, $\mathbf{Z}_g''$. Then, the PCC current dynamics $\mathbf{i}_{\text{pcc}}$ are

$$\mathbf{i}_{\text{pcc}} = [I + (\mathbf{Y} + \mathbf{\Delta}_N)\mathbf{\Delta}']^{-1}(\mathbf{T}\mathbf{i}_2^r - \mathbf{Y}\mathbf{v}_g') \tag{14}$$

where $\mathbf{v}_g'$ is the corresponding Thevenin equivalent voltage that accompanies $\mathbf{Z}_g'$. Then, we can identify $\mathbf{Y}$ as the system to be shaped to fulfill Proposition 2, so that system $\mathbf{Y} - \mathbf{W}_{pr}$ is passive. This relationship establishes the basis for PBRC for the case under study and leads to the selection of $\mathbf{W}_{pr}$, which requires a study of possible passivity shortages in VSCs.

E. Generalized Analysis of VSCs Passivity Shortage

The presence of a passivity shortage at high frequency due to control delays in VSCs is an expected result considering feedback control limitations [31], [39]. Taking into account the control loop from Fig. 4 and (7), $\mathbf{Y}$ depends on $\boldsymbol{G}^{\mathbf{u}_{\text{pcc}} \to \boldsymbol{y}}$, which is the open-loop terminal dynamics that includes the open-loop admittance $\mathbf{G}^{\mathbf{u}_{\text{pcc}} \to \mathbf{i}_2}$, and $\boldsymbol{S}^{\boldsymbol{y}^o \to \mathbf{i}_2}$, which specifies the dynamics induced by the controller $\boldsymbol{K}$. Consequently, up to frequency[6] ω_B, the terminal dynamics are defined by $\boldsymbol{S}^{\boldsymbol{y}^o \to \mathbf{i}_2}$, and at high frequency by $\mathbf{G}^{\mathbf{u}_{\text{pcc}} \to \mathbf{i}_2}$.

The presence of time delays T_d on the control input $\mathbf{u}$ leads to limiting characteristics over $\boldsymbol{S}^{\boldsymbol{y}^o \to \mathbf{i}_2}$. As explained in [31], even the "ideal" controller cannot remove this delay and it can approximate an upper frequency bound on the closed-loop bandwidth as $\omega_{\text{Bc}} = 1/T_d$. This expression is actually derived from the limitation imposed by a real zero in the right half plane (RHP) after approximating the delay, see (6), with a first-order Pade approximant. Note that the same approximation for ZOH and sampler results in no real RHP-zero, so that the limitation is only imposed by the delay. Obviously, close to that frequency the control still affects, but it degrades, which leads to an undesired behavior and a possible passivity shortage. The size of such passivity shortage relies on the dynamic behavior of $\boldsymbol{S}^{\boldsymbol{y}^o \to \mathbf{i}_2}$, which depends on the desired performance objectives and the presence of filters in the measured variables as well as PCC voltage feed-forward. Additionally, possible phase advances in $\mathbf{G}^{\mathbf{u}_{\text{pcc}} \to \mathbf{i}_2}$ around ω_{Bc} are really helpful to avoid a passivity shortage. These conclusions will be derived later in this article with several high-order grid filters and controller designs.

IV. PBRC for Current-Controlled VSCs

A. Problem Formulation

The PBRC synthesis problem in (2) is particularized for the current controller design as depicted in Fig. 6. Hence, the multiobjective optimization problem is posed as

$$\underset{\boldsymbol{K}}{\text{minimize}} \quad \gamma = \left\| \begin{bmatrix} \mathbf{W}_1 \begin{bmatrix} \mathbf{S}_r & \mathbf{Y} \end{bmatrix} \\ \mathbf{W}_2 \begin{bmatrix} \mathbf{S}_{ur} & \mathbf{S}_{ud} \end{bmatrix} \end{bmatrix} \right\|_\infty = \|\boldsymbol{M}_s\|_\infty \tag{15}$$

$$\text{subject to} \quad \|\mathbf{M}_\Delta'\|_\infty < 1$$

[6]Frequency where $\overline{\sigma}(S^{y^o \to i_2}(j\omega))$ first crosses $1/\sqrt{2}$ from below.

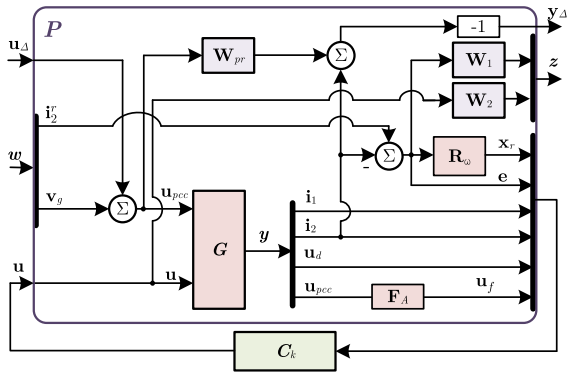

Fig. 6. PBRC problem formulation for current controller design.

where $\mathbf{S}_{ur} = [I - \boldsymbol{K}^{\boldsymbol{y}\to\mathbf{u}}\boldsymbol{G}^{\mathbf{u}\to\boldsymbol{y}}]^{-1}\mathbf{K}^{\mathbf{i}_2^r\to\mathbf{u}}$, $\mathbf{S}_{ud} = [I - \boldsymbol{K}^{\boldsymbol{y}\to\mathbf{u}}G^{\mathbf{u}\to\boldsymbol{y}}]^{-1}\boldsymbol{K}^{\boldsymbol{y}\to\mathbf{u}}\boldsymbol{G}^{\mathbf{u}_{\text{pcc}}\to\boldsymbol{y}}$, $\mathbf{S}_r = I - \mathbf{T}$, and $\mathbf{M}'_\Delta$ is the *Cayley transformation* of $\mathbf{M}_\Delta = \mathbf{Y} - \mathbf{W}_{pr}$.

The function $\mathbf{W}_1(s)$ shapes the tracking behavior over $\mathbf{S}_r$. The function $\mathbf{W}_2(s)$ defines a gain limit over functions $\mathbf{S}_{ur}$ and $\mathbf{S}_{ud}$ to constraint the achievable control bandwidth.

B. Weighting Function Selection

The transfer function $\mathbf{W}_1$ is minimum phase, it has high gain at the tracked frequency and it must ensure that $\mathbf{T}$ is close to a first-order system to properly damp reference step changes. It achieves that by shaping $\mathbf{S}_r$, and, indirectly, $\mathbf{S}_c = S^{\mathbf{i}_2^o\to\mathbf{i}_2}$ because they only differ when $\boldsymbol{K}_c^{\mathbf{i}_2\to\mathbf{u}} \neq 0$. Then, a typical standalone stability requirement, which is stability against noise and grid filter model mismatch, is $\|\mathbf{S}_c(s)\|_\infty < 6$ dB because it guarantees good general stability margins [31]. The generalized complex-valued weight in continuous-time that complies with the previous requirements is

$$\mathbf{W}_1(s) = \frac{s - j\omega_0 + \omega_B^*}{s - j\omega_0 + \omega_B^* A_o} \tag{16}$$

where $\omega_B^* \in (\omega_{\text{Bm}}, \omega_{\text{Bc}})$ is the desired closed-loop bandwidth,[7] $A_o \in (0, 1)$ is the steady-state offset, and $\omega_0 \in (-\omega_{\text{Bc}}, \omega_{\text{Bc}})$ is the tracked frequency, which is the nominal frequency of the grid considering StRF controller synthesis. This weighting function imposes $\|\mathbf{S}_r(s)\|_\infty < 1$, so that $\gamma > 1$ but it will be close to unity. The frequency ω_{Bm} is located where $\overline{\sigma}(G_g(j\omega))$ first crosses 0 dB from above. The parameter A_o can be selected arbitrarily small, however, it must be nonzero to avoid ill-conditioned optimization problems [33].

The control action weight $\mathbf{W}_2(s)$ is defined as a gain and it affects ω_B, because higher bandwidths require higher control efforts at frequencies where $\overline{\sigma}(G^{u\to y}(j\omega))$ falls. Hence, the peak values of $|\mathbf{S}_{ur}(j\omega))|$ and $|\mathbf{S}_{ur}(j\omega)|$ are at high frequency.

The weight $\mathbf{W}_{pr}$ is used to deal with cases where the uncertainty has passivity shortage. In this article, we consider cases where this happens inside a band $(\omega_{p1}, \omega_{p2})$ because of passivity shortages related to control delays in VSCs. A butterworth order one bandpass filter with gain k_{pr} is an appropriate selection. The following section defines a base case to use this weight on cases with *LCL* and *LLCL* filters. The base case is a VSC with L grid filter using current controller design without passivity enforcement in problem (15) and lower T_s.

Algorithm 1 shows a pseudocode of the controller synthesis procedure.

[7] Actually, ω_B^* is the frequency where the straight-line approximation of the weight crosses 0 dB.

TABLE II
EXPERIMENTAL SETUP PARAMETERS VALUES

Parameter[1]	Value	Unit	Parameter[2]	Value	Unit
Base power, S_b	150	kVA	L_1	500	µH
Base voltage, U_b	400	V_{rms}	L_2	250	µH
DC voltage ref.	700	V	C_f	100	µF
ω_0	$2\pi 50$	rad/s	L_3	10	µH
T_s	100	µs	C_{dc}	2.25	mF
ω_{fp}	193.6	rad/s	ω_{Bdc}	78.24	rad/s

[1] Double-update strategy, so that the switching period is 200 μs.
[2] R_1, R_2, and R_3 are estimated to be 10% of their inductive reactance at ω_0.

Algorithm 1: Generalized Controller Synthesis.

Input: Model: $\boldsymbol{G}_g$, T_s, T_d, ω_A and Design objectives: ω_0, ω_B^*, $\mathbf{W}_2$, ω_{p1}, ω_{p2}, k_{pr}, $\gamma_{\max}$.
Output: Controller gains: $\boldsymbol{C}_k$.

Define plant and weights:
$\boldsymbol{G} = \text{sysic}(\ldots, \boldsymbol{G}_g, \mathbf{G}_d)$; %Eq. (5)
$\mathbf{W}_1 = \text{ss}(\ldots, \omega_0, \omega_B^*)$; %Eq. (16);
$\mathbf{W}_{pr} = k_{pr} \cdot \text{butter}(1, [\omega_{p1}, \omega_{p2}]$, 'bandpass', 's');
Compose generalized plant:
$\mathbf{R}_\omega = ss(\ldots, \omega_0)$; %Eq. (8);
$\mathbf{F}_A = \text{butter}(1, \omega_A$, 'low', 's');
$\boldsymbol{P} = \text{sysic}(\ldots, \boldsymbol{G}, \mathbf{W}_1, \mathbf{W}_2, \mathbf{W}_{pr}, \mathbf{R}_\omega, \mathbf{F}_A)$; %Fig. 6
$\boldsymbol{P} \to P$ % Real-valued equivalent
Define controller tunable parameters:
$C_k = \text{sysic}(\ldots, \text{realp}(\ldots, K_c), \text{realp}(\ldots, G_f))$; %Fig. 4
Compose closed-loop system:
$M = \text{lft}(P, C_k)$;
Define tuning requirements and optimization:
$\text{RSOFT} = \text{TuningGoal.Gain}(w, z, 1)$;
$\text{RHARD} = \text{TuningGoal.Passivity}(u_\Delta, y_\Delta, 0)$;
$\left[\gamma, gH\right] = \text{systune}(M, \text{RSOFT}, \text{RHARD}, \ldots)$;
Evaluation of goals:
if $gH > 1$ **then**
  goto Define plant and weights;
else if $\gamma > \gamma_{\max}$ **then**
  goto Define plant and weights;
else
  return $\boldsymbol{C}_k = \text{value}(C_k)$
end if

V. RESULTS

The proposed procedure has been tested in four different cases. We have also defined a base case to illustrate a possible

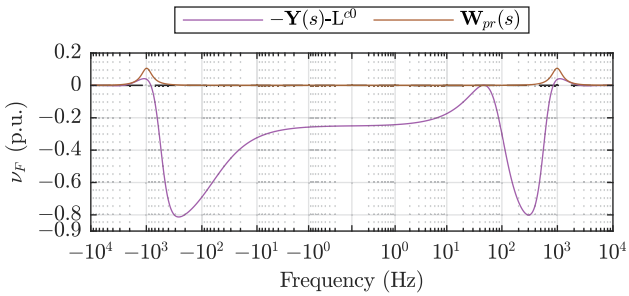

Fig. 7. IFP of $-\mathbf{Y}$ in case L^{c0} and $\mathbf{W}_{pr}$ for PBRC assessment.

passivity shortage analysis and $\mathbf{W}_{pr}$ selection. The frequency-domain results[8] will be correlated with time-domain experimental results. The plant parameters for the four studied cases are summed up in Table II. For LCL and $LLCL$ grid filters, the resonance frequency is 1.23 kHz, close to the corresponding ω_{Bc}, which is 1.59 kHz, so that it can be damped by control means. The $LLCL$ grid filter notch was placed on the first switching harmonics band, which is 5kHz.

A. Current Controller Design Cases

The base case and the four cases under study and their related labels are as follows.

1) *Case* L^{c0}: Base case of *L* filter controller synthesis without passivity enforcement. It illustrates the passivity shortage to be compensated by cases LCL and $LLCL$. The electrical parameters are expressed in Table II, considering that $T_s = 200\ \mu$s and $\omega_B^* = 521.6$ rad/s.
2) *Case* L^{c1}: *L* filter controller synthesis without passivity enforcement to demonstrate the result when there is no robustness constraint. The tunable part $\mathbf{G}_f$ is constrained to unity, which is a usual control approach to reduce the admittance magnitude, and $\omega_A = 1/T_s$.
3) *Case* L^{c2}: *L* filter controller synthesis with passivity enforcement and $\mathbf{W}_{pr} = 0$. The tunable part $\mathbf{G}_f$ has order 2 and $\omega_A = 1/T_s$.
4) *Case* LCL: *LCL* filter controller synthesis with passivity enforcement by the given $\mathbf{W}_{pr}$. The system $\mathbf{G}_f$ has order 2 and $\mathbf{D}_f = 0$. The $\mathbf{u}_{\text{pcc}}$ measurement is less noisy, so that the antialiasing filter is removed, $\mathbf{F}_A = 1$.
5) *Case* $LLCL$: *LLCL* filter controller synthesis with passivity enforcement by the given $\mathbf{W}_{pr}$. The system $\mathbf{G}_f$ is the order 2 and $\mathbf{D}_f = 0$. The $\mathbf{u}_{\text{pcc}}$ measurement is less noisy, so that the antialiasing filter is removed, $\mathbf{F}_A = 1$.

Analysis of case L^{c0} allows us to define a numerical expression for $\mathbf{W}_{pr}$, which will be used in the last two cases. Fig. 7 depicts that the passivity shortage occurs between -830 and -2600 Hz, and 850 and 2685 Hz. This passivity shortage is close to the corresponding ω_{Bc}, which is 795 Hz. According to Fig. 7, the required passivity excess for robust stability using $\mathbf{W}_{pr}$ is defined by $\omega_{p1} = 2\pi 750$ rad/s and $\omega_{p2} = 2\pi 1300$ rad/s with gain $k_{pr} = 0.07$.

[8]For the sake of clarity, frequency response of complex-valued transfer functions is displayed following a bisymmetric logarithmic transformation [40].

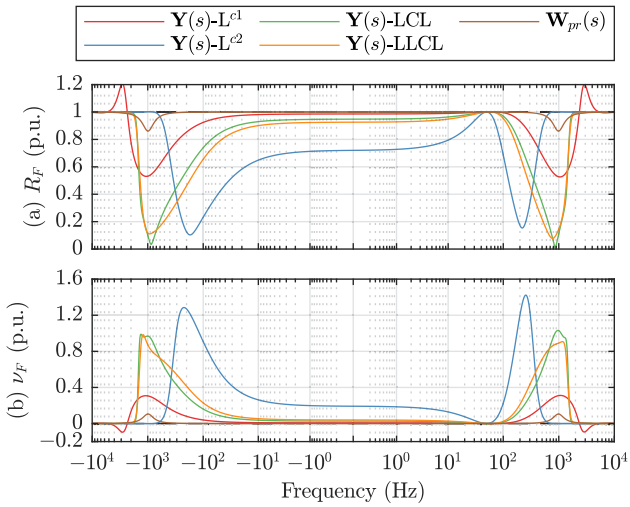

Fig. 8. Passivity indices of $\mathbf{Y}$ for each case under study. (a) *R*-index R_F. (b) IFP index ν_F.

The optimization problem (15) has been formulated with similar control objectives. This optimization minimizes $\|\mathbf{S}_r(s)\|_\infty$ and, indirectly, $\|\mathbf{S}_c(s)\|_\infty$. The shaping capabilities of $\mathbf{W}_1$ on $\mathbf{T}$ as a first-order closed-loop system allow us to define the desired bandwidth as $\omega_B^* = 2\pi 249$ rad/s. The control action parameter is set to $\mathbf{W}_2 = 0.1$. Finally, the maximum value of the parameter to be minimized is set to $\gamma_{\max} = 2$. Still, it is up to the designer decision to accept the design by evaluating the final solution at each frequency.

For nonsmooth optimization, the tunable parameters initialization is key point to find acceptable solutions. In our practical experience, at least 100 random initial values [33] ensure finding an acceptable solution. The resulting controller gains are specified in Table III.

B. Current Control Objectives Analysis

Fig. 8 shows the passivity indices that characterize the passivity-based robustness of each current controller design case. The *R*-index (see Definition 3) and IFP index (see Definition 2), as shown in Fig. 8(a) and (b), show that case L^{c1} has a passivity shortage beyond the critical frequency $\omega_{\text{Bc}} = 2\pi 1591$ rad/s at both frequency sequences. Although it naturally compensates the passivity shortage expressed by $\mathbf{W}_{pr}$ without imposing that requirement, its stability is compromised against high-frequency resonance uncertainties. Alternatively, case L^{c2} depicts a controller design that leads to a passive system at all frequencies in the expense of poorer performances, as it will be demonstrated later. The passivity excess region of this case naturally appears at midfrequencies because this case has lower bandwidth. On the other hand, Fig. 8(a) and (b) indicates that the robust stability condition for the given $\mathbf{W}_{pr}$, see Proposition 2, is accomplished by cases LCL and $LLCL$ because $\nu_F(\mathbf{Y}(s), \omega) > \nu_F(\mathbf{W}_{pr}(s), \omega)$. The excess of passivity naturally arises as a consequence of achievable bandwidth with passivity enforcement, designed controller including feed-forward, and grid filter characteristics.

TABLE III
TUNABLE PARAMETER SOLUTIONS OF SYNTHESIZED CONTROLLERS

Gain	L^{c0}	L^{c1}	L^{c2}	LCL	LLCL
$\boldsymbol{K}_c$	$\begin{bmatrix} 610.31+j112.98 \\ 0.26+j0.03 \\ 0 \\ -1.28+j0.01 \\ 0 \end{bmatrix}$	$\begin{bmatrix} 5127.2+j476.2 \\ 0.97+j0.05 \\ 0 \\ -3.78+j0.003 \\ -0.52-j0.01 \end{bmatrix}$	$\begin{bmatrix} 390+j4.33 \\ 0.38+j0.12 \\ 0 \\ -0.215+j0.12 \\ 0.6+j0.006 \end{bmatrix}$	$\begin{bmatrix} 1909.1+j186.8 \\ 0.28+j0.07 \\ -2.38+j0.03 \\ 0.5+j0.07 \\ -0.11+j0.02 \end{bmatrix}$	$\begin{bmatrix} 2299.1+j115.6 \\ 0.39+j0.12 \\ -2.66+j0.1 \\ 0.51+j0.12 \\ -0.22+j0.03 \end{bmatrix}$
$\boldsymbol{A}_f$	0	0	$\begin{bmatrix} -11933 & -9150 \\ -15257 & -15688 \end{bmatrix}$	$\begin{bmatrix} -1599.64 & -6939.57 \\ 5559.57 & -4900.84 \end{bmatrix}$	$\begin{bmatrix} -15707.96 & 15707.96 \\ -15707.96 & -15648.93 \end{bmatrix}$
$\boldsymbol{B}_f$	0	0	$\begin{bmatrix} 341.28 \\ 554.41 \end{bmatrix}$	$\begin{bmatrix} 110.13 \\ 627.03 \end{bmatrix}$	$\begin{bmatrix} -224.58 \\ 56.19 \end{bmatrix}$
$\boldsymbol{C}_f$	0	0	$\begin{bmatrix} 9.98 & -10.95 \end{bmatrix}$	$\begin{bmatrix} -2.880 & 5.441 \end{bmatrix}$	$\begin{bmatrix} 23.85 & 33.07 \end{bmatrix}$
$\mathbf{D}_f$	0	1	0.0695	0	0

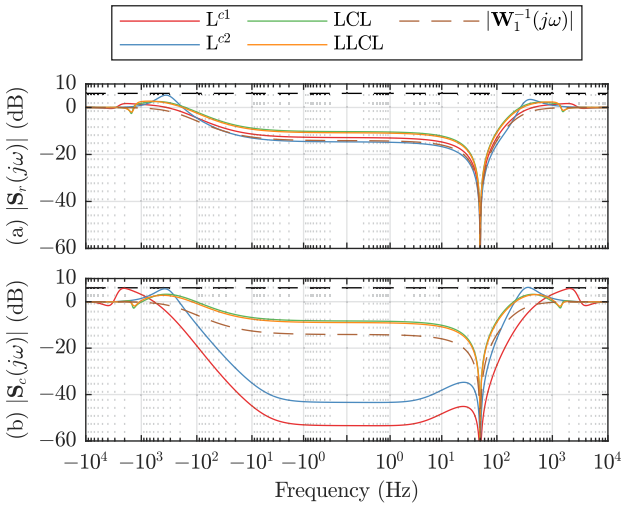

Fig. 9. Performance objective $\mathbf{W}_1^{-1}$ compared with the magnitude of (a) $\mathbf{S}_r$ and (b) $\mathbf{S}_c$.

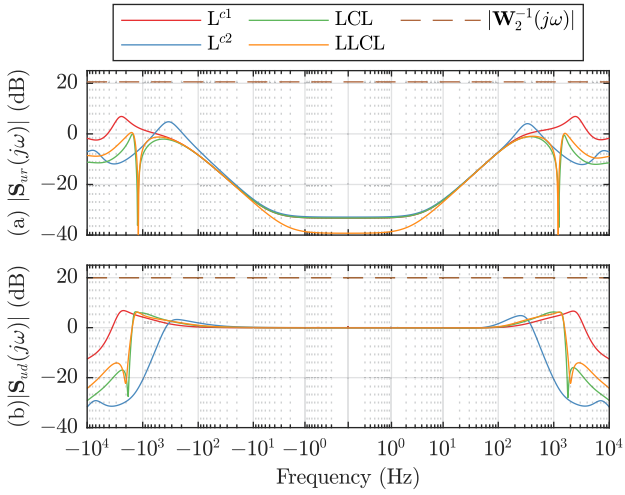

Fig. 10. Control action objective $\mathbf{W}_2^{-1}$ compared with the magnitude of (a) $\mathbf{S}_{ur}$ and (b) $\mathbf{S}_{ud}$.

Fig. 9 compares the sensitivity objective given by $\mathbf{W}_1^{-1}$ with each design. Fig. 9(a) shows that the sensitivity to reference signal $\mathbf{S}_r$ practically matches the desired tracking behavior of $\mathbf{W}_1^{-1}$. Still, case L^{c2} shows slight differences, and it will result in overshoot and lower bandwidth. Fig. 9(b) depicts the sensitivity $\mathbf{S}_c$, which is very similar to $\mathbf{S}_r$, and all cases accomplish the common design criterion to ensure standalone robustness against noise and grid filter mismatches, $\|\mathbf{S}_c(s)\|_\infty < 6$ dB. Cases LCL and $LLCL$ have similar $\|\mathbf{S}_c(s)\|_\infty$, as well as L^{c1} and L^{c2}. However, the two latter cases have a completely different performance between them.

Fig. 10 compares the control action objective given by $\mathbf{W}_2^{-1}$ with each design. It shows that case L^{c1} requires higher control action at higher frequencies to achieve good tracking performances. This high gain peak at high frequency may be related with a passivity shortage at the same frequency range, see peak value matching of $|\mathbf{S}_{ur}(j\omega)|$ and $|\mathbf{S}_{ud}(j\omega)|$ with R_F in Fig 10(a), because both sensitivities have too much gain at frequencies where the control capabilities degrade.

The Bode plots of the tracking function $\mathbf{T}$ are depicted in Fig. 11(a). Due to grid filter resonance proximity to ω_{Bc}, a low peak arises close to the resonance frequency for cases LCL and $LLCL$, but it can be considered as damped. This Bode plot also shows that case L^{c2} has worse tracking dynamics because the peak value of $|\mathbf{T}(j\omega)|$ is not placed at the tracked frequency ω_0.

Finally, the admittance $\mathbf{Y}$ Bode plots in Fig. 11(b) associate their magnitude and phase characteristics to the passivity indices in Fig. 8. On the one hand, the lower magnitude characteristic is achieved by case L^{c1}, whereas case L^{c2} has the higher magnitude and cases LCL and $LLCL$ have intermediate magnitude values. On the other hand, the associated phase characteristics show that case L^{c1} crosses $-90°$ and $90°$ at high frequency, that is a passivity shortage, while the other cases are always within that phase range. Then, we can conclude that case L^{c1} may perform better with PCC voltage dips, which is better current transients. However, its passivity shortage will lead to instability in the presence of high-frequency grid impedance resonance uncertainty, whereas the other cases are robustly stable.

Fig. 11 clearly shows the control tradeoff between performance and robust stability for the L grid filter cases L^{c1} and L^{c2}. High-order grid filters as LCL and $LLCL$ cases are a fair alternative to reach good performances and robust stability while achieving their main purpose: reducing switching harmonics. This conclusion is better understood by comparing open-loop characteristics and by recalling the analysis of $\mathbf{Y}$ in Section III-E. The gain falling of $\mathbf{G}_g^{u\to i_2}$ after the resonant frequency in *LCL* and *LLCL* filters is advantageous to force $|\mathbf{S}_c(j\omega)| = 0$ dB very

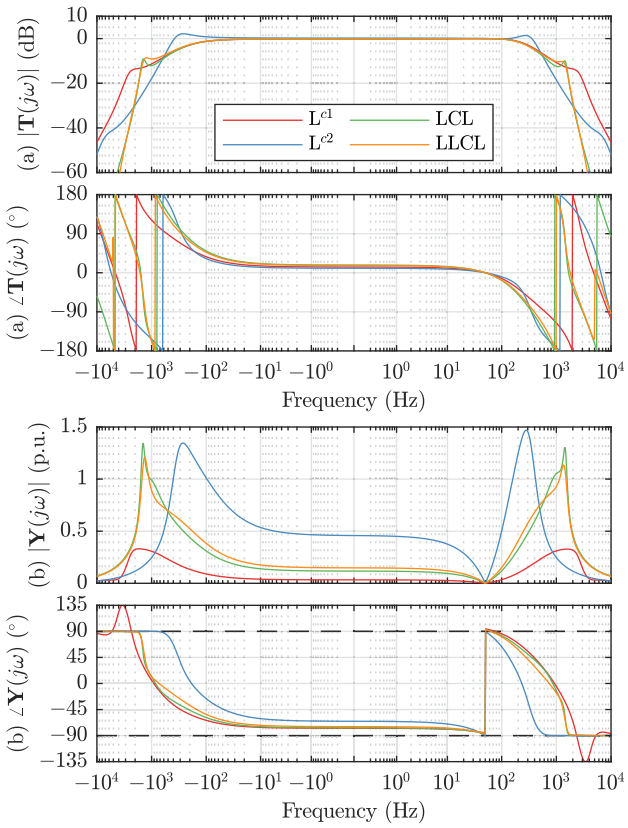

Fig. 11. Bode plots of (a) tracking $\mathbf{T}$ and (b) admittance $\mathbf{Y}$.

quickly, which naturally constrains the control action beyond that frequency, as shown in Fig. 10. Additionally, the phase advance of $\mathbf{G}^{\mathbf{u}_{\text{pcc}}\to\mathbf{i}_2}$ from its zero at the antiresonance frequency to the resonant frequency avoids that $\mathbf{Y}$ reaches $-90°$ (or $90°$ for negative sequence) close to ω_{Bc}.

Finally, Fig. 12 shows the robustness against uncertain L-type and LC-type grid impedance, $\mathbf{Z}_g(s) = sL_g$ and $\mathbf{Z}_g(s) = (sL_g)/(s^2C_gL_g + 1)$, respectively, for cases L^{c1} and LCL by depicting the roots of $[I + \mathbf{YZ}_g] = 0$. Both cases are always stable in a wide range of L_g, when $\mathbf{Z}_g$ is L-type, see Fig. 12(a) and (c). When $\mathbf{Z}_g$ is LC-type and L_g is kept constant while C_g changes, case L^{c1} becomes unstable in some C_g values, see Fig. 12(b), whereas case LCL is always stable. The placement of resonance at frequencies where L^{c1} has passivity shortage leads to its instability. Therefore, these results prove the robustness of the current controller designed in case LCL. This can be extrapolated for cases L^{c2} and $LLCL$ because they also fulfill the passivity requirement for robustness.

C. Discussion on Proposal

PBRC method ensures the robust stability of the current controllers. However, the workability of VSC requires at least an appropriate CRG to synchronize with the grid and exchange power, which inevitably changes the input admittance. Besides, in some applications, harmonic rejection is required to ensure the quality of injected currents. Then, we would like to point out the following.

1) The resulting overall input admittance Y_F changes in each operating point close to ω_0, which is unavoidable, and we can no longer ensure the robust stability of the whole system following Proposition 1. However, we can ensure the robust stability of the designed current controller by only considering Y. Besides, the passivity properties at mid and high frequency remain, so that we can still ensure the stability against high-frequency resonant uncertainty. For instance, Fig. 13 depicts the IFP of Y_F for a set of operating points in case L^{c2}, where it is noticeable how they all fit the IFP of Y (in SRF) at mid and high frequency. Note that the model Y_F is derived by linearizing the CRG, see Section III-C, in SRF following a similar approach as the one presented in [41].
2) The harmonic rejection capability is required in considerably weak grids, where the PCC voltage is very polluted with low-order harmonics. However, not all applications require this functionality. Still, the proposed method accepts the inclusion of higher order resonators inside the controller structure, parallel to $\mathbf{R}_\omega$, as shown in Fig. 4.

Both issues require dedicated studies, which can be approached within the proposed robust controller tuning methodology. The selected controller structure is one of many possibilities as well as the application.

D. Experimental Results

The experimental setup schematic is depicted in Fig. 14. The setup is composed of a three-phase 150 kVA NPC converter with the designed current controllers implemented on a DSP TMS320C6713 DSK at 225 MHz (4.44-ns cycle time). The VSC operates as STATCOM, by implementing the current reference generator algorithms in Section III-C, being v_{dc}^r and q^r specified by the user interface. The reference power, p^r and q^r, is kept below 0.3 p.u., by saturating their values because of electrical safety in our laboratory. Before entering the current controller $\boldsymbol{K}(z)$, $\mathbf{i}_2^r$ is saturated to 0.3 p.u. in order to avoid steady-state overcurrent. The grid filter parameters for the case under study are specified in Table II.

This setup allows us to prove the robust stability of the designed current controllers. However, due to the high power of the VSC and electrical safety of our laboratory, we have been unable to test close to nominal power.

The implementation of $\boldsymbol{K}(z)$ is straightforward considering each signal and gain with their real-valued version. The controller structure also facilitates the implementation of a saturator and backward calculation as antiwindup strategy. Basically, when $\mathbf{u}$ saturates to $v_{\text{dc}}/\sqrt{3}$ in magnitude, $\mathbf{x}_r$ changes its value in accordance at the following time step by adding the difference between saturated and nonsaturated $\mathbf{u}$. The backward calculation is also useful for the initialization of the system.

The grid is either generated by the programmable power supply Regatron TC.ACS.30.480.400.S.LC or the utility grid

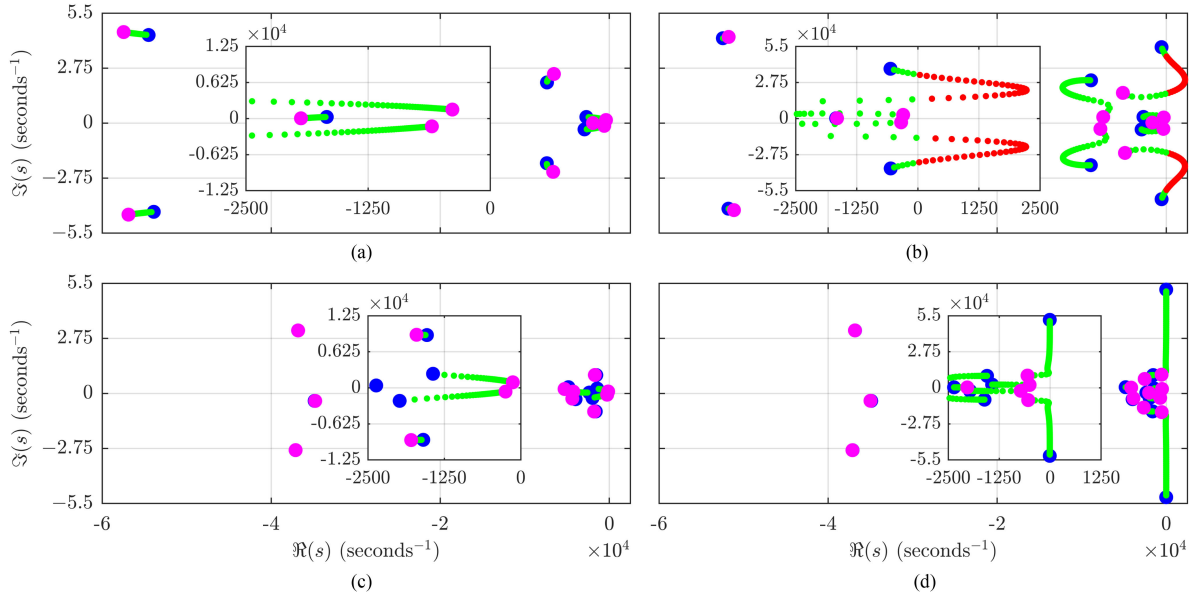

Fig. 12. Pole map evolution of $[I + \mathbf{YZ}_g] = 0$, being $\mathbf{Z}_g$ L-type, where $L_g \in [0.425, 4.25]$ mH, or LC-type, where $L_g = 0.425$ mH and $C_g \in [2.38\ 238]$ μF (from blue to magenta). Cases and type of $\mathbf{Z}_g$. (a) L^{c1} and L-type. (b) L^{c1} and LC-type. (c) LCL and L-type. (d) LCL and LC-type.

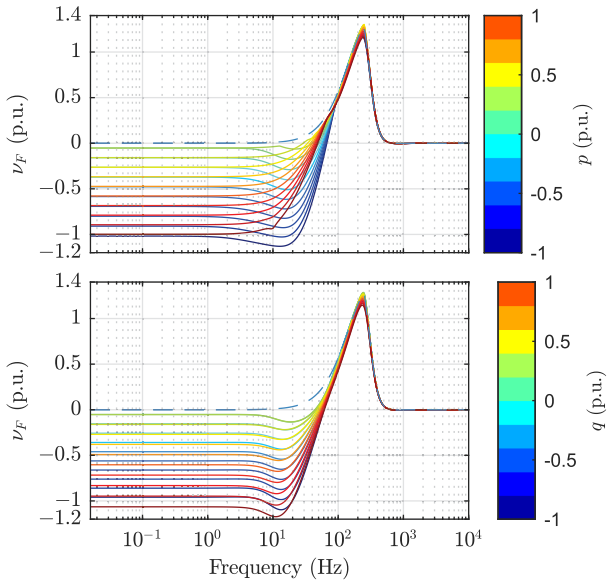

Fig. 13. For case L^{c2}, IFP index plots of Y_F in solid lines when exchanging active power p (top) or reactive power q (bottom), and Y in dashed line.

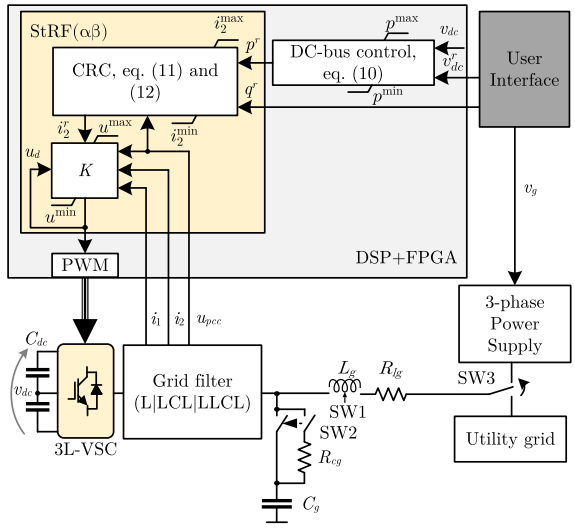

Fig. 14. Experimental setup for robust stability tests. The VSC is operating as STATCOM connected to a grid through a line with variable impedance.

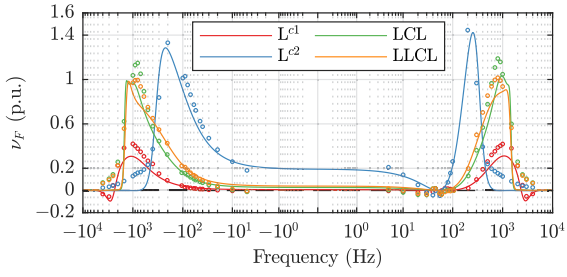

Fig. 15. Experimental input admittance IFP index with circle markers (○) compared with its corresponding theoretical one in solid line.

depending on manual switch SW3. The grid impedance is a test bench compose of a tapped inductor $L_g = \{0.425, 2.55\}$ mH, depending on manual switch SW1. This allow us to test the VSC with short circuit ratio (SCR) from strong to very weak conditions, SCR $= U_b^2/(S_b\omega_0 L_g) = \{7.98, 1.33\}$. The grid resonance is generated by closing switch SW2 and introducing a capacitor $C_g = 16.66$ μF. This switch first inserts a given damping resistor R_{cg} to energize the capacitor, which avoids overcurrent. After 10 ms, this resistor is removed.

The actual input admittance is experimentally measured by injecting a frequency perturbation with the programmable power supply. Meanwhile, the converter under measurement collects the PCC three-phase voltages and currents. Then, the fast Fourier transform is applied on the collected data. Fig. 15 depicts the

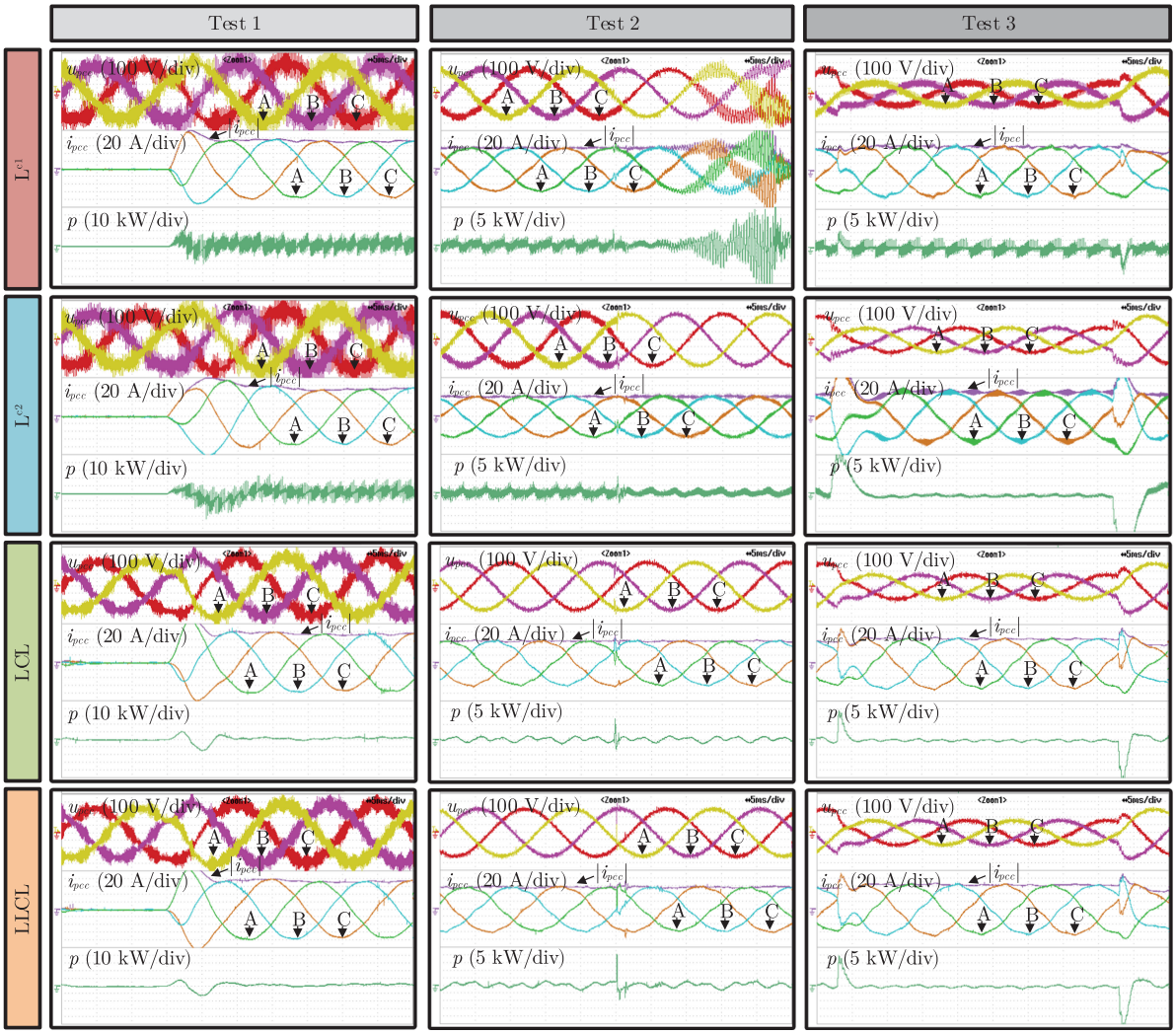

Fig. 16. Experimental results where, for each case and test, the PCC variables are depicted in each window as: Three-phase voltages u_{pcc} at the top; three-phase currents i_{pcc} and corresponding vector magnitude $|i_{\text{pcc}}|$ are depicted at the middle; active power p at the bottom.

IFP index of $\mathbf{Y}$ for each case. The experimental measurement verifies the theoretical results up to high frequency where the actual admittance has an excess of passivity due to inductors parasitic open-loop admittance behavior. Besides, the IFP close to ω_0 confirms the passivity shortage due to the inherent effect of any CRG algorithm. Still, case L^{c1} has a passivity shortage at high frequency that leads to instability, if the cable impedance has any resonance.

The experimentally measured excess of passivity, depicted in Fig. 15, of cases LCL and $LLCL$ prove that they would be able to stabilize the PCC, if a VSC with base case L^{c0} had been connected in parallel facing an LC-type grid impedance with resonance uncertainty.

Three experimental tests for each design case have been carried out and depicted in Fig. 16.

1) Reactive power reference step change from $q^r = 0\ \text{kVA}_r$ to $q^r = 40\ \text{kVA}_r$ with SW2 open and SCR $= 1.33$, that is a considerably weak grid.
2) Switch SW2 is closed to generate a grid resonance at 1.89 kHz and SCR $= 7.98$ before closing it.
3) Symmetrical 50 % voltage dip during two cycles of the fundamental sequence, i.e., 40 ms, with grid resonance, which is closed SW2, and SCR $= 7.98$. Case L^{c1} is unstable so that SW2 is open in such case.

Test 1 shows that all cases are stable with very weak grid conditions, as previously indicated by the robustness analysis in Fig. 12. The presence of grid impedance has changed the tracking function dynamics, which is the transient response, to $\mathbf{T}[I + \mathbf{YZ}_g]^{-1}$. However, they confirm the tracking bode plots in Fig. 11(a) showing that case L^{c2} has worse tracking performance than the other cases. Although the overshoot is lower than cases LCL and $LLCL$, it takes more time to reach the steady state.

Test 2 shows the instability of case L^{c1} in the presence of a grid resonance due to its high passivity shortage close to that frequency, see Fig. 8. This result was also showed by the robustness analysis in Fig. 12. The other cases are stable. These results confirm the robustness of the designed current controllers for cases L^{c2}, LCL, and $LLCL$ due to their passive properties, as shown in Fig. 8.

Test 3 demonstrates the performance characteristics toward voltage dips and their relationship with $|\mathbf{Y}(j\omega)|$, see Fig. 11(b). Case L^{c1} has a great performance toward voltage dips with a very low peak currents and active power p exchange, whereas L^{c2} has a very poor performance. This clearly reflects what has to be sacrificed in current controller designs for *L* grid filters in order to ensure robust stability. Alternatively, case LCL and $LLCL$ have a considerably good response while preserving their robust stability. Additionally, these cases are able to damp the resonance quicker than case L^{c2} when a voltage dip appears. Then, the selection of high-order grid filters is more favorable, when considering the control tradeoff between performance and passivity-based robust stability.

VI. Conclusion

The passivity-based analysis and design are a necessary approach to avoid undesired couplings and instabilities, and it is very suitable for electrical systems. This article has reviewed the possible mathematical approaches of PBRC for three-phase VSCs when dealing with complex systems and several requirements. The multiobjective tuning of controllers with a nonsmooth optimization tool has been proven to be very valuable when dealing with fixed structures, which are of interest for industrial applications.

Passivity indices are a powerful tool to ensure robust stability of the current controller. The excess of passivity, given by each current controller design, naturally arises from selected design and controller structure (including PCC voltage feed-forward), and grid filter type. At high frequency, *LCL* and *LLCL* filters are able to give the required excess of passivity because of their open-loop characteristics.

Independently of plant complexity, these design methodology and analysis are still applicable. For instance, this article has shown a complex-valued discrete-time controller design for a continuous-time plant that can be either *L*, *LCL,* or *LLCL* with additional antialiasing filter on the PCC voltage measurement. Controller structure possibilities are plentiful, and further study is required to extend the analysis to the CRG or harmonic rejection algorithms.

The experimental results show that a control tradeoff is necessary. Robust stability is achieved in the expense of poorer performances. However, the main difference of our approach with a previous analysis is that this approach looks for the most optimum design taking into account both control objectives.

Appendix
Cayley Transformation

By applying Lemma 1, the *Cayley transformation* for a generalized plant P_p is

$$P'_p: \begin{bmatrix} \dot{x} \\ y'_\Delta \\ y \end{bmatrix} = \left(\begin{array}{c|cc} A' & B'_1 & B'_3 \\ \hline C'_1 & D'_{11} & D'_{13} \\ C'_3 & D'_{31} & D'_{33} \end{array}\right) \begin{bmatrix} x \\ u'_\Delta \\ u \end{bmatrix} \tag{17}$$

where, considering $D^i_{11} = [I + D_{11}]^{-1}$, the transformation of each matrix, e.g., $A' = A - B_1 D^i_{11} C_1$, is

$$\begin{aligned} C'_1 &= -2D^i_{11}C_1 & C'_3 &= C_3 - D_{31}D^i_{11}C_1 \\ B'_1 &= B_1[I - D^i_{11}D_{11}] & B'_3 &= B_3 - B_1 D^i_{11} D_{13} \\ D'_{11} &= I - 2D^i_{11}D_{11} & D'_{13} &= -2D^i_{11}D_{13} \\ D'_{31} &= D_{31}[I - D^i_{11}D_{11}] & D'_{33} &= D_{33} - D_{31}D^i_{11}D_{13}. \end{aligned}$$

References

[1] X. Wang and F. Blaabjerg, "Harmonic stability in power electronic-based power systems: Concept, modeling, and analysis," *IEEE Trans. Smart Grid*, vol. 10, no. 3, pp. 2858–2870, May 2019.

[2] X. Wang, F. Blaabjerg, and P. C. Loh, "Passivity-based stability analysis and damping injection for multiparalleled VSCs with LCL filters," *IEEE Trans. Power Electron.*, vol. 32, no. 11, pp. 8922–8935, Nov. 2017.

[3] L. Harnefors, A. G. Yepes, A. Vidal, and J. Doval-Gandoy, "Passivity-based controller design of grid-connected VSCs for prevention of electrical resonance instability," *IEEE Trans. Ind. Electron.*, vol. 62, no. 2, pp. 702–710, Feb. 2015.

[4] L. Harnefors, X. Wang, A. G. Yepes, and F. Blaabjerg, "Passivity-based stability assessment of grid-connected VSCs—An overview," *IEEE Trans. Emerg. Sel. Topics Power Electron.*, vol. 4, no. 1, pp. 116–125, Mar. 2016.

[5] J. Sun, "Impedance-based stability criterion for grid-connected inverters," *IEEE Trans. Power Electron.*, vol. 26, no. 11, pp. 3075–3078, Nov. 2011.

[6] S. Vesti, T. Suntio, J. A. Oliver, R. Prieto, and J. A. Cobos, "Impedance-based stability and transient-performance assessment applying maximum peak criteria," *IEEE Trans. Power Electron.*, vol. 28, no. 5, pp. 2099–2104, May 2013.

[7] K. Zhou, and J. C. Doyle, *Essentials of Robust Control*, New Jersey, USA: Prentice Hall Upper Saddle River, 1998.

[8] S. Cobreces, E. J. Bueno, F. J. Rodriguez, D. Pizarro, and F. Huerta, "Robust loop-shaping H-infinity control of LCL-connected grid converters," in *Proc. IEEE Int. Symp. Ind. Electron.*, Jul. 2010, pp. 3011–3017.

[9] J. Bao and P. L. Lee, *Process Control—The Passive Systems Approach*. London, U.K.: Springer, 2007.

[10] M. G. Safonov, *Stability and Robustness of Multivariable Feedback Systems*. Cambridge, MA, USA: MIT Press, 1980.

[11] G. Zames, "On the input-output stability of time-varying nonlinear feedback systems—Part II: Conditions involving circles in the frequency plane and sector nonlinearities," *IEEE Trans. Autom. Control*, vol. 11, no. 3, pp. 465–476, Jul. 1966.

[12] W. M. Haddad and V. Chellaboina, *Nonlinear Dynamical Systems and Control*. Princeton, NJ, USA: Princeton Univ. Press, Sep. 2011.

[13] M. Xia, P. J. Antsaklis, V. Gupta, and F. Zhu, "Passivity and dissipativity analysis of a system and its approximation," *IEEE Trans. Autom. Control*, vol. 62, no. 2, pp. 620–635, Feb. 2017.

[14] M. Xia, P. Gahinet, N. Abroug, and C. Buhr, "Sector bounds in control design and analysis," in *Proc. IEEE 56th Annu. Conf. Decis. Control*, Jan.2018, pp. 1169–1174.

[15] A. J. Agbemuko, J. L. Dominguez-Garcia, O. Gomis-Bellmunt, and L. Harnefors, "Passivity-based analysis and performance enhancement of a vector controlled VSC connected to a weak AC grid," *IEEE Trans. Power Del.*, vol. 36, no. 1, pp. 156–167, Feb. 2021.

[16] L. Harnefors, X. Wang, S.-F. Chou, M. Bongiorno, M. Hinkkanen, and M. Routimo, "Asymmetric complex-vector models with application to VSC-grid interaction," *IEEE Trans. Emerg. Sel. Topics Power Electron.*, vol. 8, no. 2, pp. 1911–1921, Jun. 2020.

[17] M. Beza and M. Bongiorno, "Impact of converter control strategy on low- and high-frequency resonance interactions in power-electronic dominated systems," *Int. J. Elect. Power Energy Syst.*, vol. 120, Sep. 2020, Art. no. 105978.

[18] L. Harnefors, R. Finger, X. Wang, H. Bai, and F. Blaabjerg, "VSC input-admittance modeling and analysis above the Nyquist frequency for passivity-based stability assessment," *IEEE Trans. Ind. Electron.*, vol. 64, no. 8, pp. 6362–6370, Aug. 2017.

[19] F. Hans, W. Schumacher, S. F. Chou, and X. Wang, "Passivation of current-controlled grid-connected VSCs using passivity indices," *IEEE Trans. Ind. Electron.*, vol. 66, no. 11, pp. 8971–8980, Nov. 2019.

[20] A. Akhavan, H. R. Mohammadi, J. C. Vasquez, and J. M. Guerrero, "Passivity-based design of plug-and-play current-controlled grid-connected inverters," *IEEE Trans. Power Electron.*, vol. 35, no. 2, pp. 2135–2150, Feb. 2020.

[21] C. Xie, K. Li, J. Zou, D. Liu, and J. M. Guerrero, "Passivity-based design of grid-side current-controlled LCL-type grid-connected inverters," *IEEE Trans. Power Electron.*, vol. 35, no. 9, pp. 9813–9823, Sep. 2020.
[22] J. Perez, S. Cobreces, R. Grino, and F. J. R. Sanchez, "H-inf current controller for input admittance shaping of VSC-based grid applications," *IEEE Trans. Power Electron.*, vol. 32, no. 4, pp. 3180–3191, Apr. 2017.
[23] S. Cobreces, X. Wang, J. Perez, R. Grino, and F. Blaabjerg, "Robust admittance shaping approach to grid current harmonic attenuation and resonance damping," *IEEE Trans. Ind. Appl.*, vol. 54, no. 5, pp. 5039–5053, Sep. 2018.
[24] C. Scherer, P. Gahinet, and M. Chilali, "Multiobjective output-feedback control via LMI optimization," *IEEE Trans. Autom. Control*, vol. 42, no. 7, pp. 896–911, Jul. 1997.
[25] C. Scherer and S. Weiland, "Linear matrix inequalities in control," *Lecture Notes, Dutch Inst. Syst. Control*, Delft, The Netherlands, 2015.
[26] J. V. Burke, D. Henrion, A. S. Lewis, and M. L. Overton, "HIFOO—A MATLAB package for fixed-order controller design and H infinity optimization," *IFAC-PapersOnline*, vol. 5, no. pt 1, pp. 339–344, 2006.
[27] P. Apkarian and D. Noll, "Nonsmooth H infinity synthesis," *IEEE Trans. Autom. Control*, vol. 51, no. 1, pp. 71–86, Jan. 2006.
[28] P. Gahinet and P. Apkarian, "Decentralized and fixed-structure H-infinity control in MATLAB," in *Proc. IEEE Conf. Decis. Control*, 2011, pp. 8205–8210.
[29] P. Apkarian, P. Gahinet, and C. Buhr, "Multi-model, multi-objective tuning of fixed-structure controllers," in *Proc. Eur. Control Conf.*, Jul. 2014, pp. 856–861.
[30] J. Serrano, S. Cobreces, E. J. Bueno, and M. Rizo, "Passivity-based robust current control of grid-connected VSCs," in *Proc. IEEE Appl. Power Electron. Conf. Expo.*, Mar. 2020, pp. 745–752.
[31] S. Skogestad and I. Postlethwaite, *Multivariable Feedback Control: Analysis and Design*. New York, NY, USA: Wiley, 2007, vol. 2.
[32] J. C. Willems, "Dissipative dynamical systems part II: Linear systems with quadratic supply rates," *Archive Rational Mechanics Anal.*, vol. 45, no. 5, pp. 352–393, 1972.
[33] MathWorks, "Control System Toolbox," Sep. 2019.
[34] M. G. Safonov, E. A. Jonckheere, M. Vermaj, and D. J. N. Limebeer, "Synthesis of positive real multivariable feedback systems," *Int. J. Control*, vol. 45, no. 3, pp. 817–842, 1987.
[35] L. Hewing, S. Leonhardt, P. Apkarian, and B. J. E. Misgeld, "H-inf optimal controller design with closed-loop positive real constraints," *J. Dyn. Syst., Meas., Control*, vol. 139, no. 9, Sep. 2017, Art. no. 094502.
[36] L. Harnefors, "Modeling of three-phase dynamic systems using complex transfer functions and transfer matrices," *IEEE Trans. Ind. Electron.*, vol. 54, no. 4, pp. 2239–2248, Aug. 2007.
[37] S. Cobreces, E. Bueno, F. Espinosa, F. J. Rodriguez, and C. J. Martin, "Contributions to the DC-bus voltage controller of back-to-back voltage source converters," in *Proc. Ind. Electron. Conf.*, vol. 2005, 2005, pp. 2475–2480.
[38] H. Akagi, E. H. Watanabe, and M. Aredes, *Instantaneous Power Theory and Applications to Power Conditioning*, 2nd ed. Hoboken, NJ, USA: Wiley, 2017.
[39] K. J. Åström and R. M. Murray, *Feedback Systems: An Introduction for Scientists and Engineers*. Princeton, NJ, USA: Princeton Univ. Press, 2010.
[40] J. B. W. Webber, "A bi-symmetric log transformation for wide-range data," *Meas. Sci. Technol.*, vol. 24, no. 2, Dec. 2013, Art. no. 027001.
[41] B. Wen, D. Boroyevich, R. Burgos, P. Mattavelli, and Z. Shen, "Analysis of d-q small-signal impedance of grid-tied inverters," *IEEE Trans. Power Electron.*, vol. 31, no. 1, pp. 675–687, Jan. 2016.

Javier Serrano-Delgado (Graduate Student Member, IEEE) received the M.Sc. degree in industrial engineering in 2018 from the University of Alcala, Alcala de Henares, Spain, where he is currently working toward the Ph.D. degree in power electronics with the Electronics Engineering Applied to Renewable Energies Research Group (GEISER).

His research interests include digital control of power converters, distributed generation systems, grid-connected converters, microgrids, and renewable energy sources.

Santiago Cobreces (Member, IEEE) received the B.Sc. and M.Sc. degrees in telecommunications engineering and the Ph.D. degree in electronics engineering from the University of Alcala, Alcala de Henares, Spain, in 2003 and 2009, respectively.

Since 2012, he has been an Associate Professor with the Department of Electronics, University of Alcala, where he is also a member of Electronics Engineering Applied to Renewable Energies Research Group (GEISER). His current research interests include automatic control and system identification applied to power electronic systems power quality, and distributed power generation systems.

Mario Rizo (Member, IEEE) received the M.Sc. degree in telecommunication engineering and the Ph.D. degree in power electronics from the University of Alcala, Alcala de Henares, Spain, in 2009 and 2013, respectively.

From 2007 to 2013, he was a member of the Electronics Engineering Applied to the Renewable Energies Research Group (GEISER). He is currently with Siemens Gamesa, Madrid, Spain. His research interests include multisequence control of voltage-source converters applied to renewable energy systems, energy storage systems, microgrids, and medium-voltage multilevel converters.

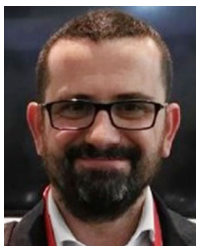

Emilio Jose Bueno (Member, IEEE) received the M.Sc. and Ph.D. degrees in electronics engineering from the University of Alcala, Alcala de Henares, Spain, in 1999 and 2005, respectively.

Since 2009, he has been an Associate Professor with the Department of Electronics, University of Alcala, and a Member of the Electronics Engineering Applied to the Renewable Energies Research Group (GEISER). From 2010 to 2013, he was a Vice-Dean of the Polytechnic School, University of Alcala, in charge of Electrical Engineering Studies. His research interests include linear control of grid converters and drives, power quality, distributed generation systems, and medium-voltage converter topologies.